MicroSoar: A New Instrument for Measuring Microscale Turbulence from Rapidly Moving Submerged Platforms

T. M. DILLON, J. A. BARTH, A. Y. EROFEEV, G. H. MAY, AND H. W. WIJESEKERA

College of Oceanic and Atmospheric Sciences, Oregon State University, Corvallis, Oregon

(Manuscript received 19 August 2002, in final form 19 February 2003)

ABSTRACT

A new high-frequency turbulence measuring instrument, MicroSoar, has been developed, tested, and used to make scalar variance dissipation rate measurements. MicroSoar was mounted on the undercarriage of SeaSoar, a depth-programmable winged platform, and towed by a ship, at speeds up to 7 kt, in a depth range of the sea surface to 120 m. Sensors carried by MicroSoar were a fast thermistor, a pressure sensor, a microscale capillary conductivity sensor, and a three-axis accelerometer. With appropriate assumptions about the local *T*–*S* relation, measurements of microscale conductivity fluctuations can often be used to directly determine temperature variance dissipation rate (χ_T), the Cox number (C_x), and the scalar diathermal turbulent diffusivity (K_T). Compared to conventional quasi-free-fall tethered vertically profiling instruments, MicroSoar's major advantage lies in its ability to sample large fluid volumes and large geographic areas in a short time, and to provide, rapidly and simply, two-dimensional (horizontal–vertical) representations of the distribution of oceanic mixing rates.

1. Introduction

Turbulent stirring and mixing processes are important mechanisms for transporting heat, salt, and mass across density surfaces in the ocean. Distributions of chemical, biological, and optical properties are also influenced by turbulence. Mixing of dissolved scalar properties must occur at very small scales, typically less than a centimeter. Therefore, observations of scalar property concentration gradients at centimeter and subcentimeter length scales are necessary for direct measurements of property transport. Modeling and understanding global-scale processes, such as climatic change, depend on our knowledge of heat transport across density surfaces in the stratified ocean (e.g., Bryan 1987). The problem of predicting climate change and temperature distributions on global length scales therefore depends on our ability to describe, in a statistical sense, the temperature distribution on length scales 10^9 times smaller than global length scales themselves.

Accurate description of oceanic diapycnal transport has, consequently, been a major goal of oceanographic research. A reliable theoretical description of oceanic turbulence is not available. Most efforts to understand turbulent mixing have been semiempirical, based on observations of the intensity and distribution of mixing events (e.g., Gregg 1987; Osborn 1980). Turbulent mixing events in the ocean are extremely intermittent, and basin-scale averages of transport are dominated by energetic events. Samples of mixing must be intensively collected over very large time- and space scales to obtain meaningful averages. The ability to accurately determine turbulent transport from small-scale measurements is therefore highly dependent on the ease and rate with which measurements can be made, and on the total volume of fluid that can be sampled in a brief period.

Measurements of oceanic turbulence have been occurring for at least the last four decades (Lueck et al. 2002). While the first attempts to measure oceanic microscale turbulence made use of a towed platform (Grant et al. 1962) using velocity and temperature sensors in the intense turbulence of a tidal channel, the ''first-generation'' instruments for general-purpose oceanic use were free-fall, internally recording, vertical profilers [see discussion in Gregg (1998)]. These devices were launched from a ship, fell freely to a predetermined depth, released a ballast weight, and then buoyantly ascended for recovery and data downloading. The main turbulence sensor was a fast-responding thermistor (a modern incarnation of which is the Thermometrics FP-07), which, because of limited frequency response, limited the fall speed to $O(0.1\ \mathrm{m\ s^{-1}})$. Total elapsed time for a cast to, say, 500 m, was roughly 4–6 h, and only a few profiles per day could be collected. The need to recover the instrument also limited operations to reasonably good weather conditions, and, usually, to daylight hours. On a 28-day research cruise, it would be possible in principle to sample 40–80 km of water, but in practice it was often less. Though the statistics ob-

Corresponding author address: Hemantha W. Wijesekera, COAS, 104 OC Admin., Oregon State University, Corvallis, OR 97331-5503. E-mail: hemantha@coas.oregonstate.edu

tained with them were not good by modern standards, these profilers provided scientists with their first good view of subsurface stratified turbulence.

The currently used ''second-generation'' microstructure profilers are tethered with a slack cable, and fall semifreely (Caldwell et al. 1985; Gregg 1976). These instruments typically fall at speeds $O(0.75\ \mathrm{m\ s^{-1}})$ and send signals through their umbilical tether for recording aboard the mother ship. The usual sensor suite includes a fast-responding thermistor, one or more airfoil shear sensors (Osborn 1980), a pressure sensor, and a conductivity sensor. A variety of additional sensors may also be used. The most significant advantages of tethered dropped instruments lie in their ability to make many profiles per day, and in their ability to provide real-time data to the operator. They may also be used in more severe weather than true free-fall profilers; the tether allows operation (ideally) whenever it is safe to be on the deck of a research ship. Although their umbilical may (rarely) foul propellers or other parts of a ship, tethered instruments remain the conventional ''workhorse'' of modern oceanic turbulence research. On a 28-day research cruise, it is possible in principle to sample of order 100 km of fluid, and make 1000–2500 casts, depending on the maximum depth sampled and the actual drop speed used. For example, Moum and Caldwell (1985) made 2200 casts, with average depth 120 m in the equatorial Pacific, and sampled about 300 km of fluid. Padman and Dillon (1991) made over 1500 casts to an average depth of 350 m while camped on an ice floe over the Yermak Plateau, sampling approximately 450 km of fluid. This is about an order of magnitude more observational information per expedition, for roughly equivalent expense and effort in terms of ship-days and man-years, than could be obtained with first-generation recovered free-fall instruments.

In this report, we describe MicroSoar, a new high-speed data acquisition and turbulence-measuring system, which is designed to improve turbulence sampling ability by another order of magnitude. MicroSoar is attached to the undercarriage of the profiling platform SeaSoar (Pollard 1986) and is towed by a research vessel at approximately $3.5\ \mathrm{m\ s^{-1}}$. The angle of attack of wings on the SeaSoar body can be controlled through a conducting cable, enabling SeaSoar to be cycled through a chosen depth range. In August 1996 and April–May 1997, MicroSoar was used to measure microscale turbulence in the Mid-Atlantic Bight during the Coastal Mixing and Optics (CMO) experiment (Barth et al. 1998; O'Malley et al. 1998). The typical depth cycle of surface to 75 m was repeated every 2 min. For comparison, a 28-day cruise could, in principle, sample a path of length 8600 km; in practice, ½ day out of every 3 days is needed for downloading raw data, yielding an expected maximum sampling path length of 7100 km. During the August 1996 CMO cruise, over 11 Gbytes (1 Gbyte $= 10^{12}$ bytes) of raw data were collected over 11 towing days, and the travel path of MicroSoar was approximately 3400 km; on the April–May CMO cruise, sampling was done on a path length of approximately 5000 km, and 16 Gbyte of raw data were collected. The total time spent towing MicroSoar during these two experiments was approximately 25 days, and the total fluid path length traversed was approximately 8400 km. MicroSoar had no malfunctions during these cruises, although one sensor set was destroyed during recovery in moderately high seas and was replaced. We consider that our design objective, an order of magnitude increase in microstructure sampling capability, has been achieved.

2. Design characteristics

a. General description

MicroSoar is contained in an anodized aluminium (alloy 7075 T-6) pressure case with an inside diameter of 15.2 cm (6″), outside diameter of 17.8 cm (7″), and a length of 67.3 cm (26.5″). Sensors are mounted on the forward end cap, and connectors for power, control, and data transmission are located on the rear end cap. The pressure limit for the case is approximately 8900 psi, equivalent to 6000-m depth. The recommended safe operating limit is 1000-m depth and is determined by sensor O-ring pressure limitations.

MicroSoar is mounted on the undercarriage of SeaSoar, in place of SeaSoar's usual ballast weight (Fig. 1). MicroSoar's nosecone contains approximately 30 kg of lead ballast (because it is otherwise almost neutrally buoyant). Power is supplied through SeaSoar's tow cable, which is also used for powering and communicating with other SeaSoar sensor systems [conductivity–temperature–depth profiler (CTD), control systems, etc.]. A subset of data (typically, 1-s averages of all signals) is sent to the surface vessel for real-time monitoring; during the CMO experiment, raw data could not be transmitted in real time because communication channels were in use for other purposes.

All computational and control functions are carried out by stackable system components with a PC/104 form-factor (3.8″ × 3.6″ × 5/8″ board dimensions). MicroSoar is controlled with a 486 DX2-66 single-board computer. Two 16-bit analog-to-digital converters (ADCs) are used for data acquisition. They each have eight differential channels and operate at a maximum speed of 100 000 conversions per second. One ADC samples eight ''slow'' channels (at 256 samples per channel per second), and the other samples three ''fast'' channels (at 2048 samples per channel per second). Two hard disk drives are used for data storage, giving 3.8 Gbyte of formatted data storage availability. A four-channel I/O card is used for serial communications, an Ethernet board is used for networking in the laboratory and data downloading in the field, and a video controller card is added for bench-top diagnostics and software development.

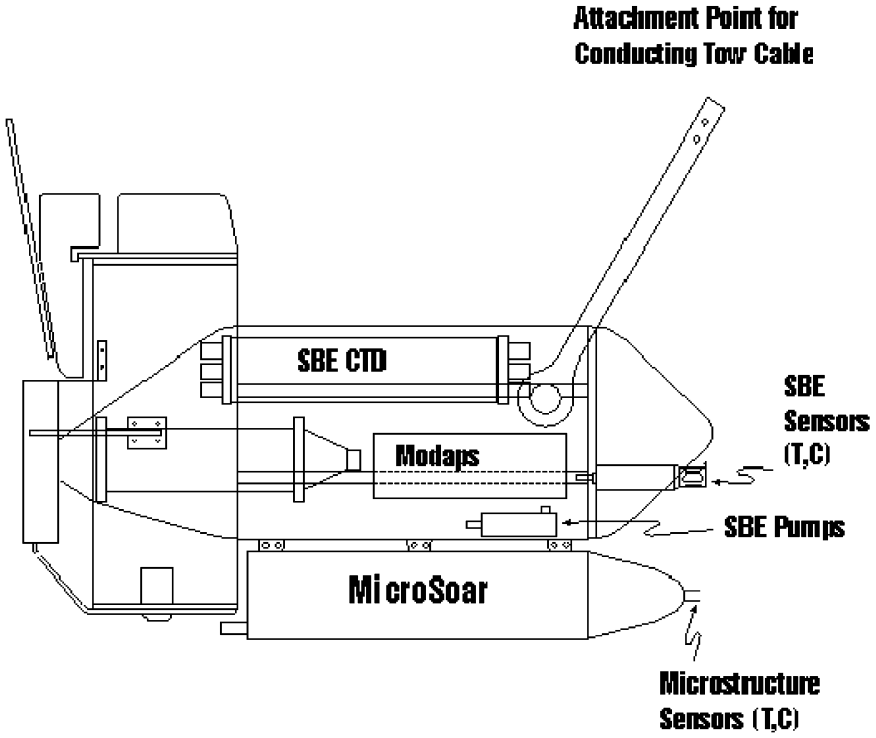

FIG. 1. Schematic diagram of MicroSoar attached to SeaSoar.

b. Sensors

The sensors on MicroSoar (Table 1) include a Thermometric FastTip FP07 thermistor, a pressure sensor, a Capillary MicroConductivity Sensor (CMCS; Paka et al. 1999), and a three-axis accelerometer. Analog sensor drivers, filters, and amplifier systems are mounted on an aluminium plate parallel to the pressure case axis and are shielded from the digital system by a metal housing (May 1997; Erofeev et al. 1998). The analog systems occupy approximately 1/3 of the pressure case volume, and are connected to the digital compartment with electromagnetic interference (EMI) filters (May 1997).

1) CAPILLARY MICROCONDUCTIVITY SENSOR (CMCS)

The CMCS (Fig. 2) concentrates an electric field between two concentric stainless steel electrodes, separated by an insulating material (epoxy) in such a manner that all conducting flux lines between the electrodes must pass through a small hole (1.5-mm diameter) at the sensor tip. The inner electrode is a long, cylindrical, stainless steel capillary tube, similar to a hypodermic needle. It is exposed to seawater through the sensor tip and is recessed approximately 1 mm from the tip. The nonconducting recessed region ensures that all electric field lines exiting the tip are parallel to the sensor body. The outer electrode is a cylinder (14.4-mm diameter, 20 cm long) with a tapered section 7.5 mm long ending 10 mm from the insulated tip. Shielded wire connects the electrodes to their analog driver circuitry. The CMCS was designed to minimize polarization effects by maximizing electrode surface area, while retaining a very small sensitive volume (Paka et al. 1999; May 1997).

The CMCS total impedance is a sum of the impedance inside the sensor's recessed tip and its external impedance. Since there is no flow through the sensor interior, impedance changes are controlled by the molecular diffusion of heat and salt into its internal cavity, and by

TABLE 1. MicroSoar sensor specifications. Time (space) resolution refers to the approximate 3-db point.

Variable	Sensor	Range	Resolution	Time (space) resolution	Sample rate
Conductivity	Capillary MicroConductivity	3–4 S m^{-1}	2×10^{-4} S m^{-1}	5×10^{-4} s (5×10^{-4} m)	2048 s^{-1}
Temperature	Thermometrics FastTip FP07	4°–24°C	0.0003°C	0.05 s (0.2 m)	256 s^{-1}
Pressure	Endevco 8510B	0–350 db	0.1 m	0.1 s (0.1 m)	256 s^{-1}
Acceleration	IC Sensors 3140-002	± 9.81 m s^{-2}	1.5×10^{-4} m s^{-2}	0.004 s (0.01 m)	256 s^{-1}

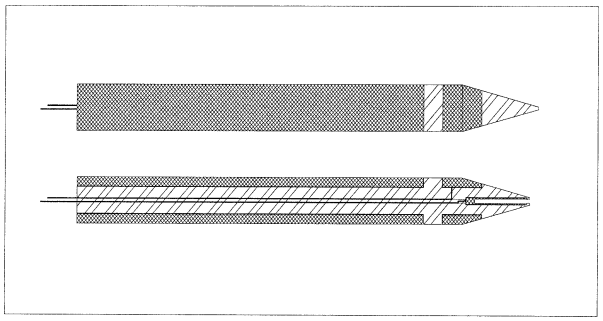

FIG. 2. Schematic diagram of the CMCS used during the CMO cruises: (top) sensor as it appears; (bottom) cut-away view of the CMCS. Cross-hatched areas are stainless steel; line-hatched areas are composed of epoxy insulation.

diffusion of heat through the sensor body, while the external impedance is controlled by conductivity fluctuations in the free-stream flow. The internal impedance is inherently a time–frequency phenomena, while the exterior impedance is a spatial-wavenumber characteristic.

The calibration of the CMCS is found by comparing its output, averaged over 1 s, to the conductivity measured by a CTD installed on SeaSoar. The high-frequency calibration of the CMCS is therefore somewhat different from the calibration at low frequency, because of the differing frequency responses of the CMCS internal and external impedance.

This effect was investigated in the laboratory by first stabilizing the sensor in a saltwater bath, and then quickly dropping it into a tank having a different salinity and the same temperature; the sensor's position and fall speed were monitored by video camera during the procedure. The response to a sudden change of salinity shows three distinct stages (Fig. 3). The first stage (a rapid, but not instantaneous change for time $t < 0.02$ s) is due to the speed of emersion, because several millimeters of the outer electrode must be in contact with saltwater before a normal response is possible. The second stage ($0.02 \text{ s} \leq t \leq 0.2$ s) is controlled by the external impedance and is a relatively flat response at 80% of full scale. The final stage ($t > 0.2$ s) is strongly affected by diffusion of saltwater into the sensor's inner cavity, changing the internal impedance. We emphasize that our approach of determining frequency response and the suggested correction for estimating χ_T (see below) are semiquantitative.

The effects of salt diffusion into the internal cavity are not noticeable before 0.2 s, and the full-scale response (99.9%) is reached after 20 s. These timescales are determined by the size of the recessed cavity and the diffusivity of salt. The diffusion timescale for $O(1$ mm) cavity is about 100 s, which is larger than the relaxation time of the internal impedance observed during the laboratory experiment. Since the salt diffusivity is approximately one-tenth of the heat diffusivity, equivalent timescales for temperature fluctuations are one-

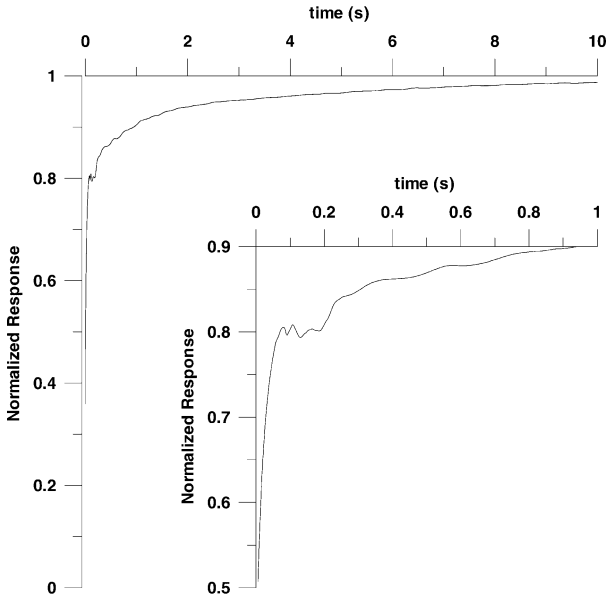

FIG. 3. Response of the conductivity sensor to sudden immersion into a saline tank. The scale is expanded in the lower plot and shows a flat response at 80% of full scale for times shorter than 0.2 s.

tenth of the timescales for salt diffusion. We assume that diffusion of heat into the inner cavity has little effect before 0.02 s, and that a near-full-scale response to temperature fluctuations will occur after approximately 1 s. This indicates that the amplitude of temperature fluctuations at frequencies above 50 rad s^{-1} (=8 Hz) will be underestimated by approximately 20%. At a tow speed of 3.5 m s^{-1}, 8 Hz corresponds to a wavelength of 0.07 m, and since the most important contributions to the temperature variance dissipation rate (χ_T) occur at smaller scales, χ_T will be underestimated by a factor of $(0.8)^2$; a simple and adequate correction can be made if χ_T is multiplied by a factor of $(1/0.8)^2 \approx 1.5$.

The spatial response of the CMCS was estimated by finding the electric field $U(r, x)$ with a finite-element numerical integration of Laplace's equation in cylindrical coordinates with axial symmetry. The governing equation for the electric field $U(r, x)$ is

$$\frac{1}{r}\frac{\partial}{\partial r}\left(r\frac{\partial U}{\partial r}\right) + \frac{\partial^2 U}{\partial x^2} = 0, \tag{1}$$

where r is the radius and x is the axis passing through center of the probe. Boundary condition at the inner conductor ($r = r_i$) is set to $U = 1$ V and that at the outer conductor [$r = r_o(x)$] is set to $U = 0$. We used a ''shareware'' version of QuickField to solve (1) (available online at http://archives.math.utk.edu/). The CMCS's potential field is nearly inversely proportional to distance from the sensor tip (Fig. 4). At the tip, the impedance has dropped to 27%. A further factor-of-2 drop, to 36.5%, occurs at 2 mm from the tip. Less than 10% of the response remains affected by fluctuations occurring farther than 1 cm from the tip. The off-axis

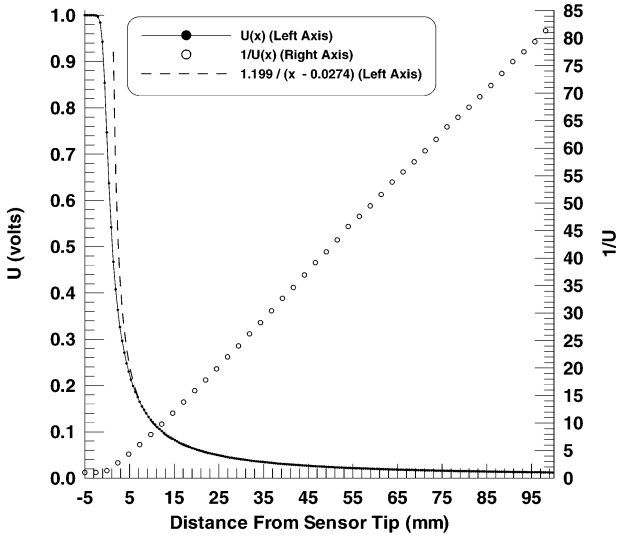

FIG. 4. Electric potential along the axis of the CMCS, obtained from a finite-element numerical solution with boundary conditions of $U = 1$ on the interior conductor, $U = 0$ on the exterior conductor, and $U = 0$ asymptotically far from the sensor (1 m). Sensor tip is at position $x = 0$, and the end of the interior electrode is at $x = -1$. Approximately 73% of the potential is lost inside the sensor, between the end of the interior electrode and the sensor tip. Potential is 0.73 V at $x = 0$, falling to 0.365 V (½ tip voltage) at $x = 2$ mm, to 0.269 V at $x = 4$ mm (e-folding length), and to 0.073 V (1/10 tip voltage) at $x = 1.67$ cm.

potential distribution is quite similar to the axial distribution but tends to experience attenuation somewhat more rapidly than in the axial direction. The e-folding length scale associated with the modeled response is about 4 mm (Fig. 4), which in turn implies that the CMCS can easily resolve 250 rad m^{-1} fluctuations.

The circuitry used to drive the CMCS supplied a 2.0-V peak-to-peak square wave to the electrodes in a driven-bridge configuration (May 1997). The bridge voltage was rectified, amplified, and electronically filtered at 1 kHz. Laboratory tests showed improved stability when the driving frequency was large (May 1997), and that even at 10 kHz, polarization effects were apparent. A driving frequency of 100 kHz was chosen to minimize polarization error, subject to the constraint of using standard, readily obtainable circuit components (May 1997).

The temperature gradient noise spectrum of the CMCS and associated circuitry is nearly proportional to frequency (Fig. 5) and can be empirically described by

$$N_{C'}(f) = N_0(f/f_0)^n, \tag{2}$$

where f is frequency, $f_0 = 1$ Hz, $n = 1.3$, and $N_0 = 5.71 \times 10^{-10}$ [(S m^{-2})^2 (cps)$^{-1}$]. In an environment of constant salinity (e.g., 34 psu at 10°C), this noise level would be observed, in temperature units, as $(\partial T/\partial C|_{S=34\text{psu},T=10°\text{C}})^2 N_0 = 3.8 \times 10^{-8}$ (°C m^{-1})^2 (cps)$^{-1}$. For comparison with other devices, the temperature-equivalent rms noise in the 1–100-Hz band is 4.2×10^{-4}°C. At our vehicle speed of 3.5 m s^{-1}, the equivalent noise in the 1–100 cpm wavenumber band, which encompasses most of the microstructure bandwidth, is 5.1×10^{-4}°C.

The CMCS was calibrated by comparing it with the SeaBird CTD normally carried by SeaSoar. The comparison was done every 5 min during the CMO cruise, by performing a least squares fit to 1-s averages of MicroSoar and CTD conductivity measurements. Some drift over periods of many hours to days was seen, presumably due to chemical changes in the CMCS interior conductor. Postcruise inspection of the CMCS revealed some thin, irregular rust-colored deposits on the interior electrode surface, possibly caused by corrosion of the electrode's stainless steel alloy. The alloy used in the Russian-manufactured CMCS is unknown. Emersion and soaking tests in a saltwater bath have shown that similar colored deposits accumulate on stainless steel alloy 304. No corrosion, and only a small amount of flocculation within the saltwater bath, was observed while performing a similar test with stainless steel alloy 316. Because of the potential for CMCS calibration drift, we think that it is unwise to use the CMCS as the primary sensor for determining salinity, unless some calibration standard, such as a CTD, is simultaneously used for comparison.

2) TEMPERATURE AND PRESSURE SENSORS

The temperature probe, built at Oregon State University (OSU), utilizes a Thermometrics series FP07 glass-coated bead thermistor. The response of the thermistor is limited to frequencies less than about 30 Hz (e.g., Vachon and Lueck 1984). A vented stainless steel sleeve protects the thermistor tip during handling and use and does not disturb the flow experienced by the thermistor, as long as the angle of attack is 30° or less, which is satisfied for all of our SeaSoar operations. The pressure sensor, used to monitor depth, is an Endevco model 8510B 500 PSIG piezoresistive pressure transducer with a sensitivity of 0.5 mV psi^{-1}.

3) ACCELEROMETERS

MicroSoar uses a three-axis accelerometer (IC Sensors model 3140-002) to monitor platform vibrations. The accelerometers have a response bandwidth of 0–500 Hz, and a two-gravity full-scale range (Table 1). Since SeaSoar vibrates energetically when being towed, acceleration was measured to determine the extent of vibrational noise. The vibrational contamination of small-scale high-frequency measurements of scalar variables arises chiefly from sensor displacements. MicroSoar's typical sensor displacement, within a 1-s interval, is O(1 mm) or less (Fig. 6), compared to the CMCS's O(3 mm) averaging length (Fig. 4), and the vibrational displacements are not an important factor. We can further demonstrate from displacement spectra shown in Fig. 7 that the vibrational contamination is

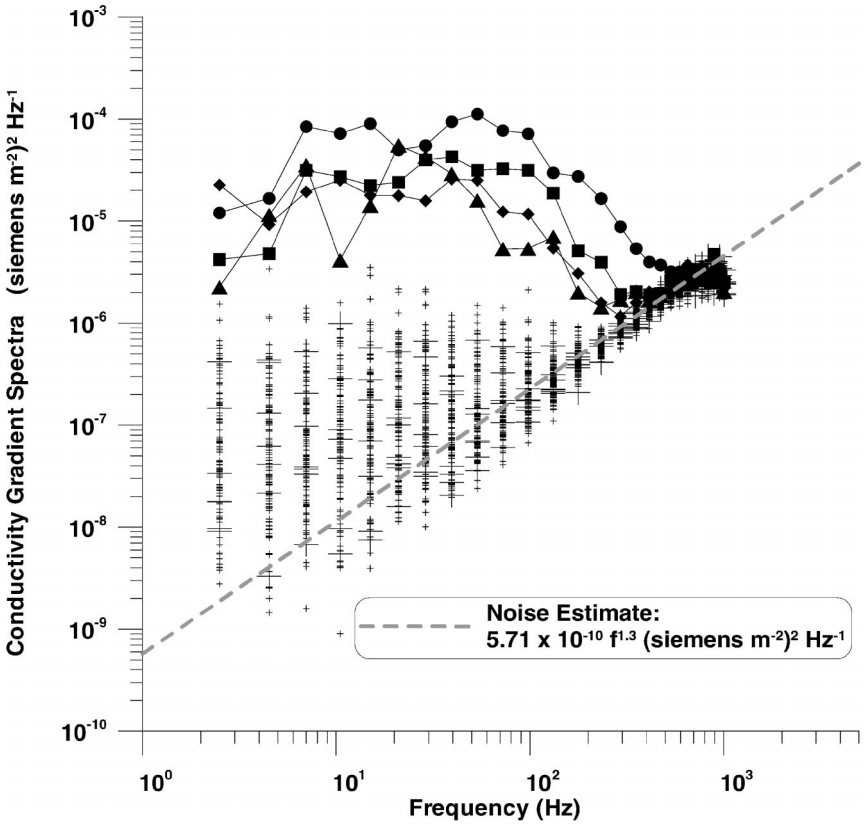

FIG. 5. One-dimensional frequency spectra of $\partial C/\partial l$ (where l is in the direction of travel) collected during the spring 1997 CMO cruise. The "+" symbols are from low-signal regions; other symbols are from four sequential high-signal regions. The dotted line is a least squares fit to the spectrum of electronic noise.

not a significant issue for the scalar measurement. The major vertical vibration is a bump at 10 Hz with displacement of 10^{-10} m^2 Hz^{-1} (Fig. 7). Then the conductivity signal due to vibrational contamination is about 10^{-10} $(0.1T_z)^2$ S^2 Hz^{-1}, where T_z is the background temperature gradient. For a typical background vertical temperature gradient of 0.1°C m^{-1}, the resultant conductivity signal is 10^{-14} S^2 Hz^{-1}, and the gradient signal is about 4×10^{-11} (S m^{-1})^2 Hz^{-1}, which is significantly smaller than the noise level shown in Fig. 5.

Measuring microscale velocity from SeaSoar would be a much more daunting task than measuring scalar variables, for here the platform velocity itself is of vital importance. The rms vibrational velocity over a 1-s interval is $O(10^{-3}$ m s$^{-1})$ (Fig. 6). The scale necessary to measure velocity microstructure is $O(\upsilon\varepsilon)^{1/4}$, where ε is the kinetic energy dissipation rate and υ is the kinematic viscosity. Over a typical range of oceanic dissipation rates, the microscale velocity ranges from 10^{-3} to 10^{-4} m s^{-1}. We conclude that, while accurately measuring microscale scalars from SeaSoar is not very difficult, the outlook for measuring microscale velocity is, at best, problematic.

3. Microconductivity as a measure of temperature

Temperature (T) can be found from conductivity (C) if salinity (S) and pressure (P) are known using the international equation of state for seawater (EOS-80; UNESCO 1981). Taylor series expansion of $T(C, S, P)$ gives

$$\delta T(C, S, P) = \alpha_{TC}\delta C + \alpha_{TS}\delta S;$$

$$\alpha_{TC} = \left(\frac{\partial T}{\partial C}\right)_{S,P}; \qquad \alpha_{TS} = \left(\frac{\partial T}{\partial S}\right)_{C,P}; \quad \text{(3a)}$$

$$\delta T(C, S, P) = \frac{\alpha_{TC}\delta C(x, y, z)}{[1 - \alpha_{TS}\gamma_{ST}(x, y, z)]};$$

$$\gamma_{ST}(x, y, z) = \left[\frac{\Delta S(x, y, z)}{\Delta T(x, y, z)}\right]. \quad \text{(3b)}$$

Here, α_{TC} (or α_{TS}) is calculated from well-known empirical relations formulated in EOS-80, while holding S and P (or C and P) constant. When the measured T–S relation is locally linear, $\delta S = \gamma_{ST}\delta T$, where γ_{ST} is the measured local slope of the T–S curve, averaged over a few meters. We assume that the local meter-scale T–

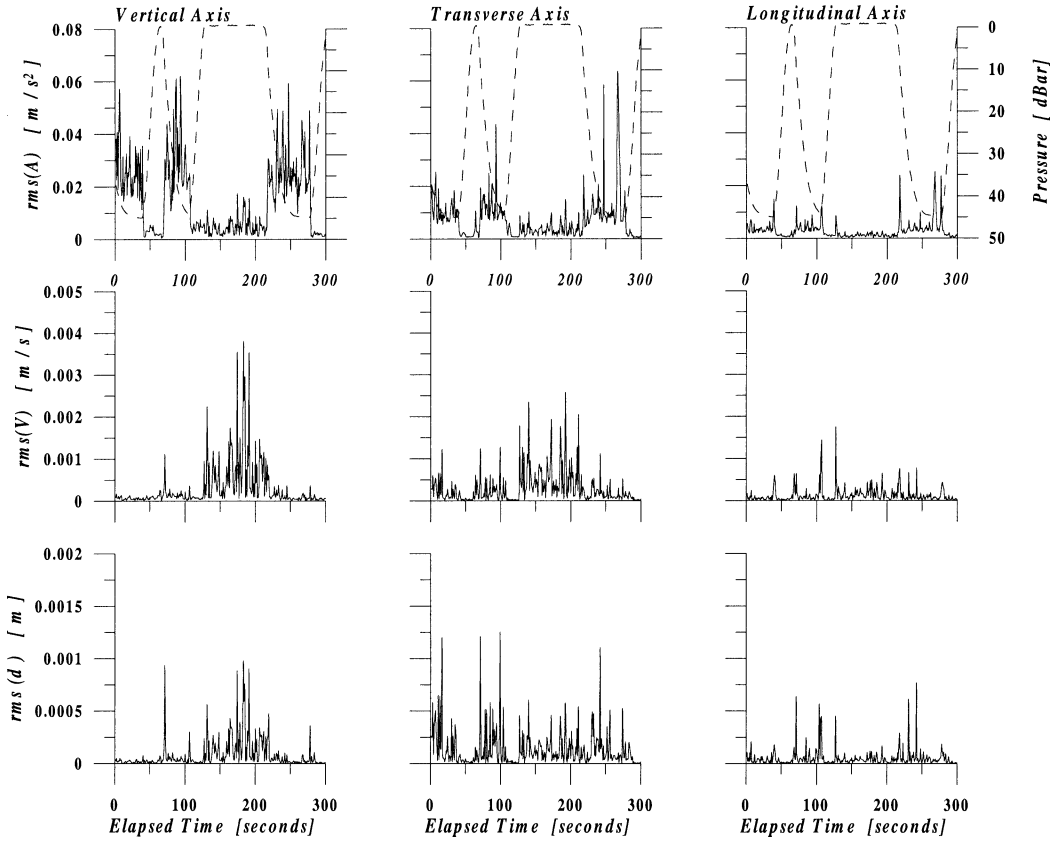

FIG. 6. Acceleration, velocity, and displacement (solid lines) and pressure (dashed lines) for one 5-min period. Root-mean-square values are calculated over a 1-s time interval. ''Vertical'' and ''transverse'' directions are perpendicular to SeaSoar's path, while ''longitudinal'' direction is along SeaSoar's path. Mean tilt of SeaSoar was not removed. Note that the vertical components contain more motion than transverse and longitudinal directions. The largest velocity and displacement fluctuations occur in the vertical direction while SeaSoar is near the surface. Displacement fluctuations over 1-s time interval are usually less than 1 mm.

S relation also holds at small scales, and find temperature fluctuations from conductivity fluctuations using (3b).

Practical use of (3) requires that $(\alpha_{TS}\gamma_{ST})$ be sufficiently different from unity. We define a ''figure of merit,'' $\Phi_M(x, y, z)$, as the local slope of the *T–C* diagram:

$$\Phi_M(x, y, z) = \left[\frac{\delta T(x, y, z)}{\partial C(x, y, z)}\right] = \frac{\alpha_{TC}}{[1 - \alpha_{TS}\gamma_{ST}(x, y, z)]}. \quad (4)$$

When $\Phi_M = O(\alpha_{TC})$, temperature fluctuations can be well defined by conductivity fluctuations. If, however, when $\alpha_{TS}\gamma_{ST} = O(1)$, then $\Phi_M \gg \alpha_{TC}$, and salinity controls conductivity more strongly than does temperature. Since $\alpha_{TS} = O(-1°\text{C psu}^{-1})$, salinity's influence on microscale conductivity can never be ignored in cases where $\gamma_{ST} = O(-1 \text{ psu } °\text{C}^{-1})$. A pathological case arises when $\alpha_{TS}\gamma_{ST} \gg 0$, $\Phi_M \ll 0$, because fluctuations of temperature and salinity may actually compensate each other's effects on conductivity (Nash and Moum 1999), unless δT and δS are uncorrelated. Since measurements show that δT–δS correlations may be high even when γ_{ST} is negative (Nash and Moum 1999), we think it unadvisable to use (4) whenever $\Phi_M \ll 0$.

The smallest scales to which fluctuations of a scalar property $\mathcal{P}$ will persist is determined by the Batchelor wavenumber (Batchelor 1959; Dillon and Caldwell 1980):

$$k_{BP} = \left(\frac{\varepsilon}{\upsilon D_{\mathcal{P}}^2}\right)^{1/4}, \quad (5)$$

where $D_{\mathcal{P}}$ is the molecular diffusivity of property $\mathcal{P}$, υ is the kinematic viscosity, and ε is the turbulent kinetic energy dissipation rate. Since the diffusivity of temperature (D_T) is $O(100)$ times larger than the diffusivity of salinity (D_s), the Batchelor wavenumber for salinity (k_{BS}) is $O(10)$ times larger than the Batchelor wavenumber for temperature (k_{BT}). It is therefore possible for the conductivity gradient variance to be dominated by salinity, rather than by temperature, in some situa-

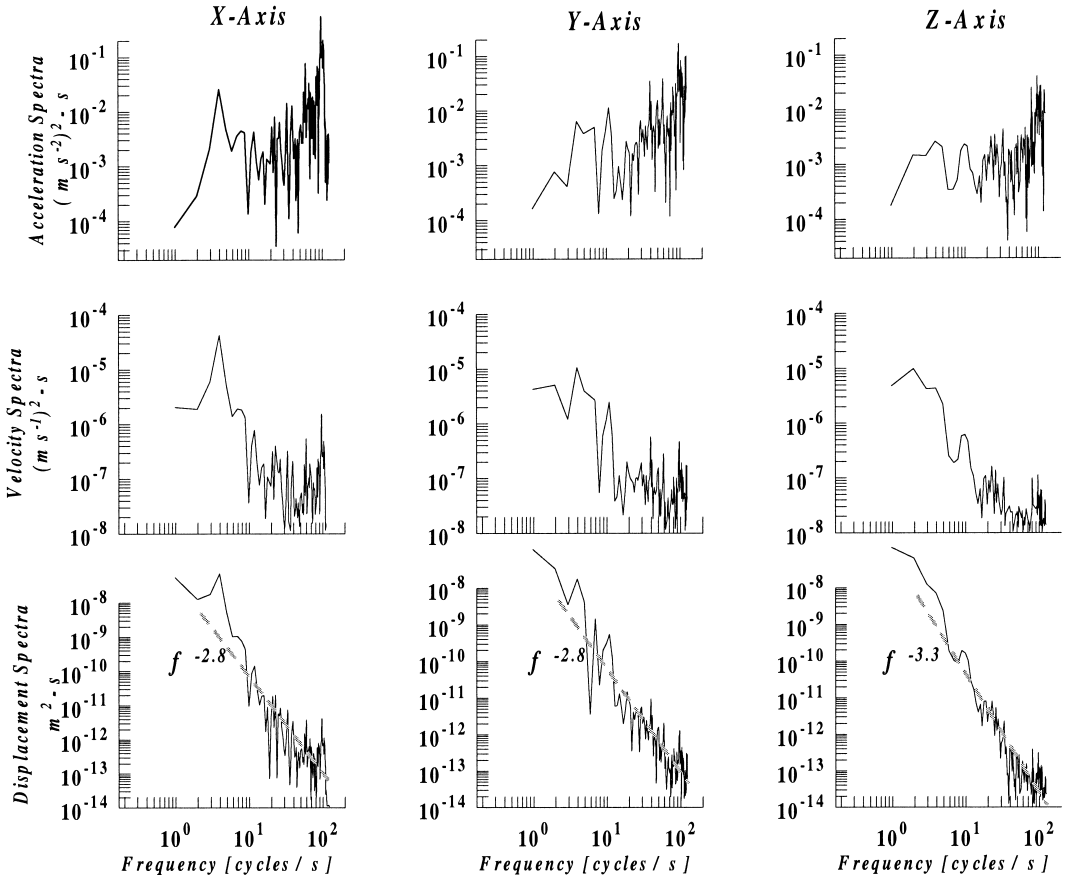

FIG. 7. Spectra of three components of acceleration, velocity, and displacement in vertical, transverse, and longitudinal directions. Acceleration spectra are (roughly) proportional to frequency, while velocity is proportional to f^{-1}, and displacement is proportional to f^{-3}. The only source of vibrational contamination for a scalar measurement, such as conductivity or temperature, arises from sensor displacements, which decrease rapidly with increasing frequency. Root-mean-square displacements in the microstructure frequency band are negligible, allowing high-frequency scalar measurements to be accurately accomplished. Velocity measurements from SeaSoar, however, are at best problematic because the velocity fluctuations are not negligible with respect to expected velocity microstructure.

tions (Nash and Moum 1999). In these cases, the CMCS microconductivity sensor is not useful, because its spatial resolution is insufficient to measure salinity fluctuations at the smallest scales.

4. Estimating turbulent transport from microconductivity

Spectra of microscale conductivity gradient can be used to determine the temperature spectrum when it is appropriate to use (3b). Typically, we find the conductivity gradient spectral peak slightly broader than would be expected from an ideal Batchelor spectrum (Batchelor 1959; Dillon and Caldwell 1980) because of conductivity's sensitivity to salinity as well as to temperature (Washburn et al. 1996). The saline sensitivity can be quantified, and corrections can be applied (Washburn et al. 1996; Nash and Moum 1999), as long as the *T–S* relation is relatively smooth, and $\Phi_M = O(\alpha_{\rm TC})$. We assume hereafter that these conditions apply, and that temperature fluctuations can be accurately obtained from (3).

The temperature variance dissipation rate (χ_T), Cox number (C_x), turbulent temperature diffusivity (K_T), and the diathermal heat flux ($\mathbf{F}_H$) can be calculated from temperature measurements along any linear path length l, as long as the smallest-scale structures are isotropic:

$$\chi_T = 2D\langle \nabla T' \cdot \nabla T' \rangle \cong 6D_T \left\langle \left(\frac{\partial T'}{\partial l} \right)^2 \right\rangle; \quad (6)$$

$$C_X = \frac{\langle \nabla T' \cdot \nabla T' \rangle}{\langle \nabla T \rangle \cdot \langle \nabla T \rangle} \cong 3 \frac{\langle (\partial T'/\partial l)^2 \rangle}{\langle \partial T/\partial z \rangle^2}; \quad (7)$$

$$K_T = \frac{1}{2} \frac{\chi_T}{|\nabla T|^2} \approx 3D_T \frac{\langle (\partial T'/\partial l)^2 \rangle}{|\partial T/\partial z|^2}; \quad (8)$$

$$\mathbf{F}_H = -K_T \langle \nabla T \rangle \cong -3D_T \frac{\langle (\partial T'/\partial l)^2 \rangle}{\langle |\nabla T| \rangle^2} \langle \nabla T \rangle; \quad (9)$$

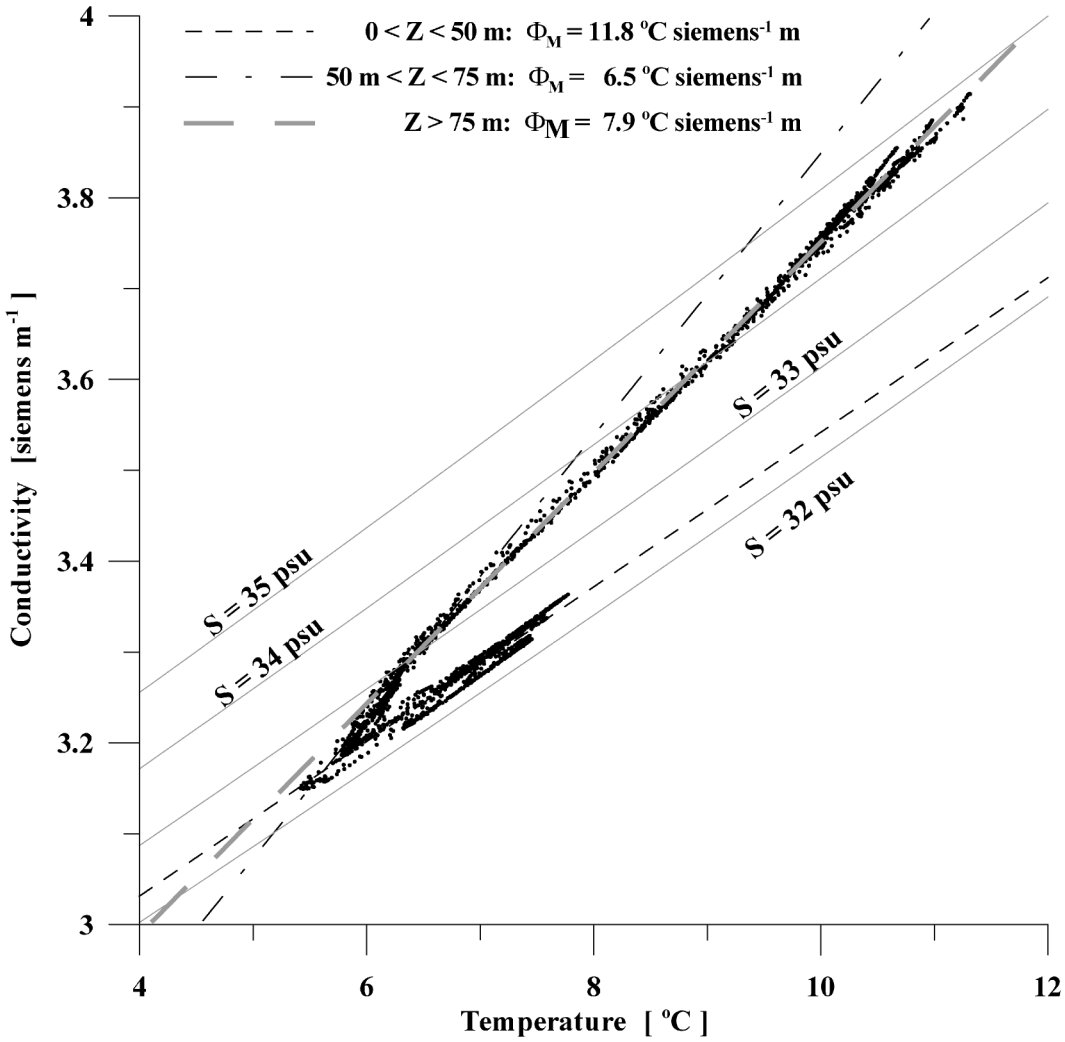

FIG. 8. A *C–T* diagram from the spring 1997 CMO cruise, along a cross-shelf path. There are three distinct regions in which Φ_M is nearly constant. In the near-surface layer (0–50 m, typical Mid-Atlantic Bight shelf water), Φ_M = 11.8°C S^{-1} m. In a deeper, warmer, and saltier water mass (from approximately 75-m depth to near bottom, apparently originating from the continental slope), Φ_M = 7.9°C S^{-1} m. An intermediate transition layer, with Φ_M = 6.5°C S^{-1} m, separates the upper shelf water and the deeper slope water. Note the abruptness of the change from upper layer to the intermediate layer, indicating that the volume of fluid containing the inflection point in $C(T)$ is very thin; typically, it is O(1 m) thick, and sometimes even thinner.

where $T' = T - \langle T \rangle$, $\langle\ \rangle$ denotes averaged over the path length, and z is the vertical coordinate. It is inadvisable to estimate χ_T directly from the arithmetic variance of $\partial T/\partial l$ because electronic noise will sometimes dominate at large frequencies. More accuracy is obtained by integrating the temperature gradient spectrum over a signal-dominated spectral band and discarding variance due to noise. It is also necessary to consider salinity's effect on high-wavenumber conductivity, even when $\Phi_M = O(\alpha_{\rm TC})$. Using the Batchelor spectrum as a first-order, or ''benchmark,'' approximation of an arbitrary scalar gradient spectrum, it is seen that most of the variance occurs for wavenumber $k < 0.1k_{\rm BP}$ (Dillon and Caldwell 1980; Nash and Moum 1999).

Nash and Moum (1999) found a high correlation between S and T for $k < 0.1k_{\rm BT}$. They also pointed out that it is often possible to neglect salinity fluctuations, because salinity's contribution to the conductivity gradient variance occurs at wavenumbers a decade larger than does temperature's contribution. They verified that reasonable estimates of χ_T could be obtained by integrating the conductivity spectrum up to $k = 0.1k_{\rm BT}$, neglecting all higher wavenumbers. Our estimates of χ_T are obtained by integrating the conductivity gradient spectrum, $\Phi_{C'}(f)$, in the range 1 Hz $< f <$ 500 Hz, subject to the condition that $\Phi_{C'}(f)$ be above electronic noise level given in $N_{C'}(f)$ [Eq. (2)]. This frequency band corresponds to the wavenumber band 0.3 cpm $< k <$ 150 cpm, and will resolve χ_T whenever 10^{-10} m^2 s$^{-3} < \varepsilon < 10^{-7}$ m^2 s^{-3}. A higher limit, say

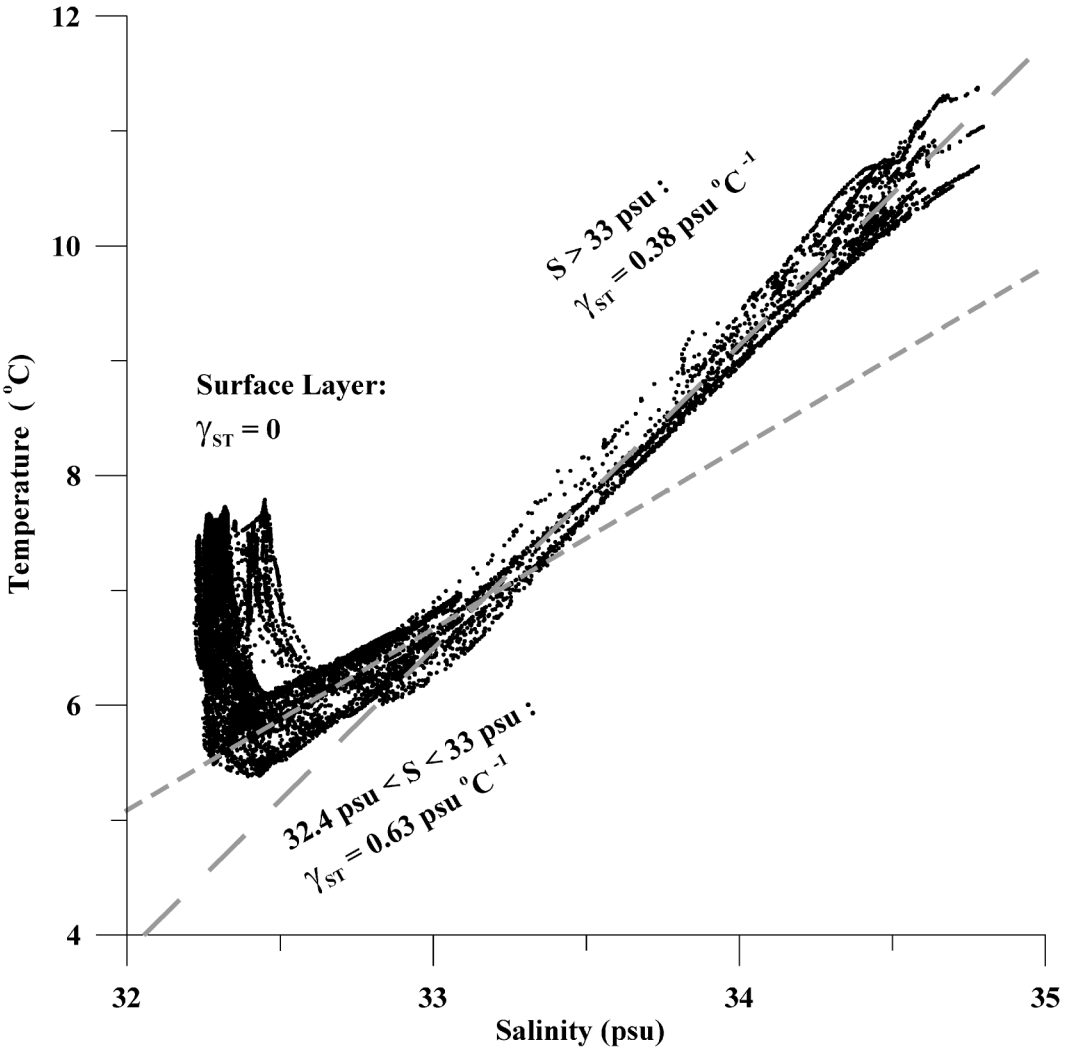

FIG. 9. A *T–S* diagram from same data as in Fig. 8. There are three distinct layers with differing *T–S* properties. Salinity is nearly constant with depth in the surface layer (shelf water) and changes horizontally in the cross-shelf direction. In the deepest layer, which originates on the continental slope, $\gamma_{ST} = 0.38$ psu °C^{-1}. In the intermediate layer, at 50–75 m, γ_{ST} is about 0.63 psu °C^{-1}. As the inflection point is approached from the surface layer, the slope γ_{ST} rotates from near zero, through $-\infty$ to $+\infty$, and then to a finite nearly constant value in the intermediate layer. The volume in which this transition takes place is very thin.

to $\varepsilon = 10^{-5}$ m^2 s^{-3}, could be used by adjusting the upper integration limit and correcting for the sensor's spatial response; however, it would be risky to raise the limit without ensuring that salinity fluctuations are not interpreted as temperature fluctuations. A better procedure would be to integrate out to $k = 0.1k_{BT}$, but that choice is not available to us because ε is not measured from MicroSoar.

5. Applicability of the microconductivity method

On the shelf of the Mid-Atlantic Bight, we observed three distinct Φ_M regimes (Fig. 8). The salinity was nearly constant in the upper 50 m, where 32.25 psu $< S <$ 32.4 psu (Fig. 9); here, $\gamma_{ST} \approx 0$, and $\Phi_M = 11.8$°C S^{-1} m. Below 70-m depth, $\gamma_{ST} = 0.38$ psu °C^{-1}, and $\Phi_M = 7.9$°C S^{-1} m. In the intermediate water, between 50- and 75-m depth, $\gamma_{ST} = 0.63$ psu °C^{-1}, and $\Phi_M = 6.5$°C S^{-1} m. In all of these cases, $\Phi_M = O(\alpha_{TC}) = O(10$°C S^{-1} m). A significant feature occurs at the boundary between the surface and intermediate layers: The *C–T* slope abruptly decreases and an inflection point exists in the *T–C* and *T–S* diagrams (Figs. 8, 9). The occurrence of an inflection point is inevitable whenever $\gamma_{ST}(x, y, z)$ becomes less than -1 while passing from one water mass to another.

No information about χ_T can be obtained from microconductivity measurements in the presence of an inflection point in the *T–C* relation (Fig. 8). In the CMO observations, the volume of water containing an inflec-

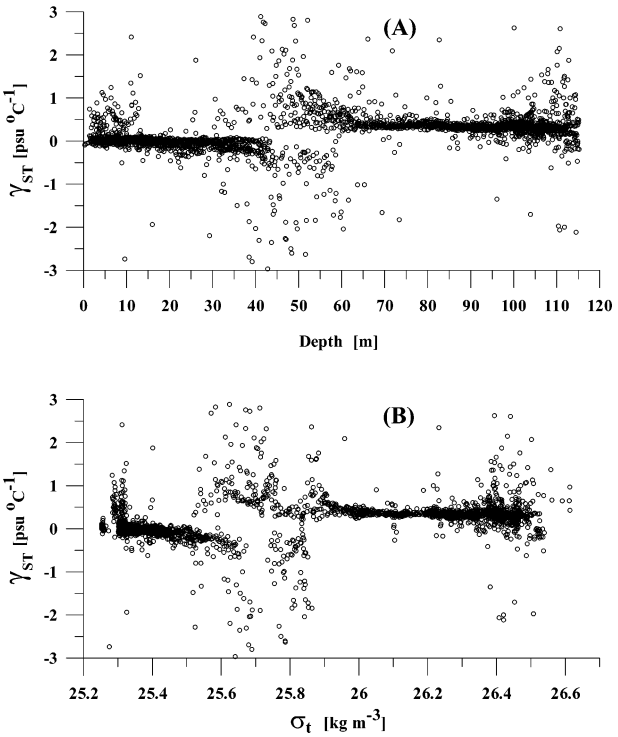

FIG. 10. The *S–T* slope γ_{ST} as a function of (a) depth and (b) density for 13 km of continuous towing at 40°N, 69.9°W, near the shelf–slope break. Note the clear separation of water masses near $\sigma_t = 25.5$ kg m^{-3}. Very large negative values of γ_{ST} in the upper layer are the result of very well-mixed volumes and turbulent overturns in which the averaging interval (i.e., 1 s, or about 1 m vertically and 3–4 m horizontally) was not sufficiently large to allow stable *T–S* gradients to be established; similar behavior can be seen when the bottom mixed layer was sampled. Note the small density thickness ($\Delta\sigma_t$) in which γ_{ST} changes from $0 \rightarrow -\infty \rightarrow +\infty \rightarrow$ (small positive values). Examination of individual profiles shows $\Delta\sigma_t \approx 0.05$ kg m^{-3}. In these volumes of rapidly changing *S–T* slope, no reliable estimates of temperature microstructure can be made because temperature and salinity have compensating influences on conductivity.

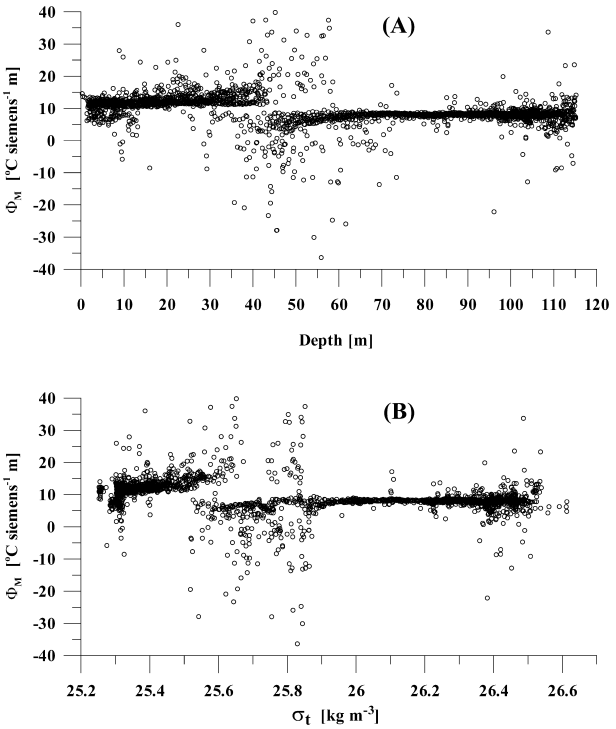

FIG. 11. The Φ_M as a function of (top) depth and (bottom) density for the same data as in Fig. 10. Few occurrences of $\Phi_M < 0$ are found. Most examples of $\Phi_M < 0$ occur in the surface and bottom mixed layers, where both δT and δC are sometimes too small to yield a stable estimate of Φ_M. However, near 50-m depth, there exists some significant instances of small or negative Φ_M that correspond to the inflection point in Figs. 8 and 9. In these cases, no estimate of temperature turbulence variables can be obtained from microconductivity measurements. Note that the shelf water mass ($\Phi_M > 9$°C S^{-1} m) is distinctly different and separated from the slope water mass ($\Phi_M < 9$°C S^{-1} m).

tion point is small and, in most cases, has a vertical extent *O*(1 m). Processes occurring in these volumes may be significant, because mixing of water masses with distinctly different *T–S* properties occurs here first. The microconductivity method of estimating temperature variance dissipation rate, Cox number, diffusivity, and fluxes of heat, salt, and mass fails at precisely these extremely interesting inflection points. However, knowledge of mixing processes very near these points can be obtained, as long as Φ_M is sufficiently well defined.

The applicability of the microconductivity method for estimating turbulence parameters in the CMO data can be seen by examining γ_{ST} (Fig. 10) and Φ_M (Fig. 11). A clear separation of surface layer (shelf water) and deeper water masses (slope water and an intermediate or transition layer) is apparent when γ_{ST} is viewed as a function of density (Fig. 10). Near the intermediate density ($\sigma_t \approx 25.55$ kg m^{-3}), γ_{ST} becomes less than -1, and (in principle) must continue to decrease until reaching -4, whereupon it changes to $+4$. It then rapidly decreases within the intermediate transition layer.

The conversion of water masses due to turbulent mixing, and possibly double-diffusive processes, must be occurring within the transition layer. It is important to note that, in almost all cases, the microconductivity method proves useful within this layer. The behavior of Φ_M reveals a well-defined ''gap'' near the transition depth (Fig. 11, top); the separation of properties is even more apparent when viewing Φ_M as a function of density (Fig. 11, bottom).

We choose a limit (somewhat arbitrarily) of $\Phi_M > 4$°C S^{-1} m for useful microconductivity measurements. Approximately 6% of samples do not satisfy this criterion (Fig. 12). Approximately 4.5% of these are samples from surface and bottom boundary layers, where gradients of *S, C,* and *T* are too small to make stable estimates of Φ_M using 1-s averages. Of all samples within the transition layer, approximately 1.5% satisfy $\Phi_M < 4$°C S^{-1} m; such samples cannot be used to deduce microscale temperature fluctuations from microconductivity measurements. The remaining 98.5% of samples

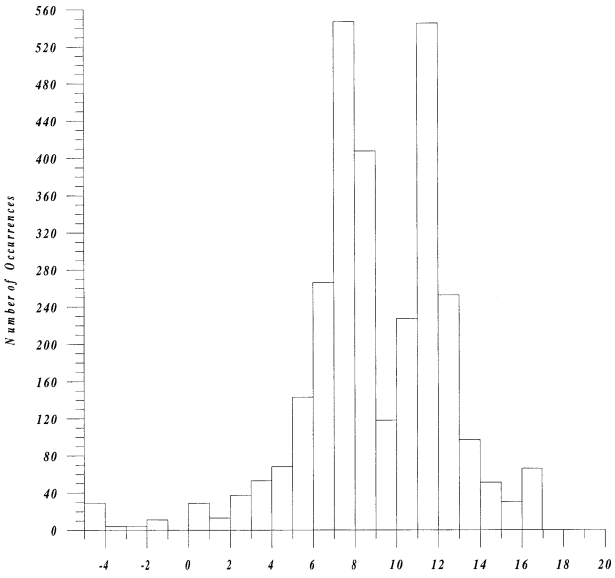

FIG. 12. Histogram of Φ_M. Approximately 2% of samples have $\Phi_M < 0$, 3% have $\Phi_M < 2°C\ S^{-1}$ m, and 6% have $\Phi_M < 4°C\ S^{-1}$ m. Note the bimodal nature of the distribution, caused by distinctly different *T*–*S* properties in the surface layer and deeper water.

either have $\Phi_M > 4°C\ S^{-1}$ m, or lie in well-mixed surface and bottom boundary layers. We believe that for 94% of all our samples, accurate estimates of temperature microstructure can be made from microconductivity measurements, as long as care is taken to ensure that integration of the conductivity spectrum is limited to wavelengths larger than 0.007 m (Nash and Moum 1999).

6. Observations of mixing parameters

While it is not our goal in this work to fully discuss the meaning and implications of our turbulence measurements, it is useful to present some preliminary results. We have been able to collect, for the first time, large-scale synoptic measurements of fully resolved small-scale scalar turbulence variables. As an example, Fig. 13 shows one latitude–depth (*y*–*z*) field of temperature, salinity, χ_T, Cox number, and heat flux, measured during the spring 1997 CMO experiment (Barth et al. 1998; Erofeev et al. 1998; O'Malley et al. 1998). The ability to make surveys of scalar turbulence over large spatial scales provides a unique opportunity to view oceanic mixing as a function of large-scale hydrography.

The temperature salinity and density (σ_t) sections (Fig. 13) show a cold wedge of shelf water (identifiable by $S < 32.6$ psu) that was, presumably, once well-mixed. Springtime surface heating has partially restratified the surface water, and a well-mixed layer ($T > 7.5°C$, depth < 20 m) lies above a weak diurnal thermocline. A deeper mixed layer, presumably a relic of prior surface heating and wind-driven mixing, is separated from the interior by a strong developing seasonal thermocline ($\sim 20\ \text{m} < z < 40$ m depth; $6.5°C < T < 7.5°C$). The near-shore water is well mixed from the seasonal thermocline to the bottom shoreward of 40.45°N. Seaward of 40.45°N a warm, salty, wedge-shaped volume of water can be seen, apparently intruding from near the continental shelf–slope water mass ($S > 32.6$ psu, $T > 7°C$). Farther offshore, the slope water mass shallows, until it surfaces near 39.8°N latitude (May 1997). The stratification separating shelf and slope water masses is strong, and isosurfaces of temperature, salinity, and density are extremely convoluted.

The χ_T section (Fig. 13) shows strong mixing occurring at the base of the surface mixed layer, and at the seasonal thermocline. It also shows a ''branching'' structure at ~40.6°N, where the seasonal and the diurnal thermoclines appear to diverge. Solely by looking at the stratification, one might expect that mixing is confined to the diurnal thermocline, but this is clearly not the case, because χ_T is also large within the seasonal thermocline seaward of 40.6°N. It is also a surprise to find another branch of high χ_T separating from the seasonal thermocline (40.5°N, ~40-m depth), deepening, and meeting with a very high χ_T layer near the bottom (~40.45°N), where the shelfwater intersects with the deeper slope water intrusion. On and within the intrusion (between 40.45° and 40.2°N; $50\ \text{m} < z < 75$ m), we also see intense mixing. Within the slope water mass (latitude less than 40.2°N; $S > 32.6$ psu) can be seen large numbers of irregularly distributed intensely mixing patches. The Cox number section (Fig. 13, bottom panel) displays the same features, with large C_x in the surface layer, the bottom layer of shelf water ($y <$ 40.45°N), and the slope water at the shelf–slope break (i.e., $S > 32.6$ psu, $y < 40.45$°N). The diffusivity in these locations often falls in the range of $O(0.7 \times 10^{-4}\ \text{m}^2\ \text{s}^{-1})$ to $O(14 \times 10^{-4}\ \text{m}^2\ \text{s}^{-1})$.

The large C_x found near the shelf–slope break is especially significant. Diffusivities here are often as large $10 \times 10^{-4}\ \text{m}^2\ \text{s}^{-1}$, and sometimes much larger. As a comparison, typical midocean thermocline diffusivity values are $O(0.1 - 0.05 \times 10^{-4}\ \text{m}^2\ \text{s}^{-1})$ (Ledwell et al. 1993; Toole et al. 1994). Our observations near the mid-Atlantic shelf–slope break are a factor $O(100)$ larger than the midocean thermocline diffusivity. Other observations of microstructure near topographic irregularities have also shown very large mixing rates (Padman and Dillon 1991; Wijesekera et al. 1993; Gregg 1998).

7. Summary and conclusions

We have designed, developed, and used a robust, versatile, high-speed underwater data acquisition system, ''MicroSoar,'' configured initially with a capillary microconductivity sensor, finescale temperature sensor, pressure sensor, and a three-axis accelerometer. MicroSoar was mounted on the undercarriage of

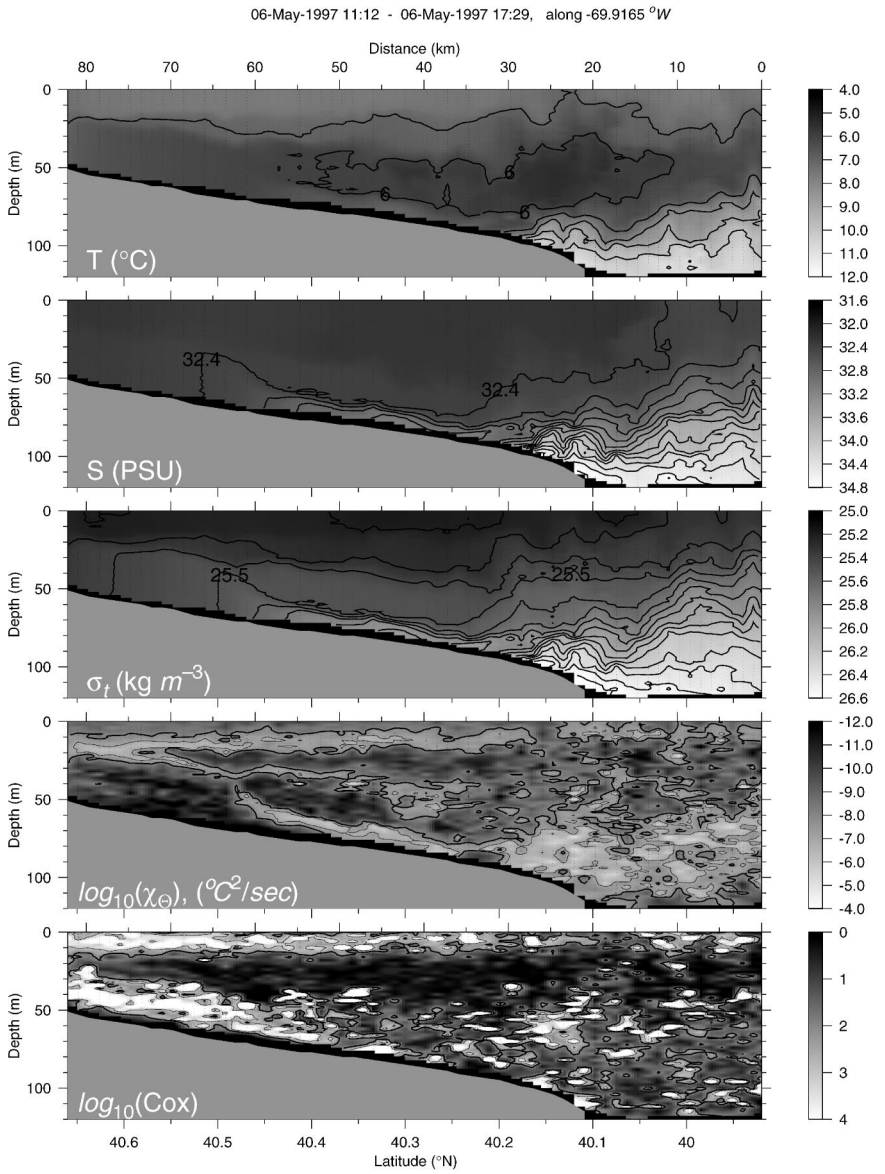

FIG. 13. Section across the shelf of the Mid-Atlantic Bight taken during the CMO experiment, 6 May 1997. First three panels (T, S, and σ_t) are from SeaSoar CTD; bottom two panels (χ_T and Cox number) are from MicroSoar. Contour intervals of T, S, and σ_t are 1°C; 0.4 psu, and 0.2 kg m^{-3}, respectively. The thick and thin lines in $\log_{10}(\chi_T)$ represent -8 and -7 contours, respectively. The thick and thin lines in $\log_{10}$(Cox) represent 2 and 3 contours, respectively. The χ_T and Cox number are very large in the surface and bottom mixing layers, in the frontal zone near the continental shelf break, and within a near-bottom intrusion extending seaward from the shelf break to 40.5°N. Cox numbers are very large beneath the thermocline shoreward of the intrusion, indicating vigorous turbulent mixing; but because the temperature gradient there is small, χ_T is small, and little heat transport occurs here.

SeaSoar, a depth-programmable winged platform, and was used to measure microscale turbulence in the Mid-Atlantic Bight during CMO experiment while towing at speeds up to 7 kt in a depth range of the sea surface to 120 m. We have been able to resolve conductivity fluctuations (e.g., Fig. 5) as small as the diffusive temperature cutoff. We have demonstrated that MicroSoar, configured with a capillary microconductivity sensor, is hardened enough, and robust enough, to make routine measurements of scalar turbulence in coastal water. MicroSoar can be towed at 3–4 m s^{-1} (or even higher than is possible with SeaSoar towing operations) without loss of small-scale resolution. With appropriate assumptions about the local T–S relation, measurements of microscale conductivity fluctuations can often be used to directly determine temperature variance dissi-

pation rate (χ_T), the Cox number (C_x), and the scalar diathermal turbulent diffusivity (K_T) (e.g., Fig. 13).

The ability to make large-scale synoptic surveys without loss of small-scale resolution allows a unique opportunity to see the behavior of oceanic mixing as it relates to large-scale hydrography and local forcing. Synoptic measurement of mixing on regional scales is critical for understanding variations of transport processes, and for diagnostic studies of ''hot spots,'' where much of the global diapycnal heat transport is thought to occur (Gregg 1998). We found that the mixing of shelf and slope water near the shelf–slope break is $O(100)$ times larger than in the midgyre Atlantic Ocean. While we have no direct evidence that similar mixing occurs on other shelf–slope regions, we have no reason to suspect that the Mid-Atlantic Bight is unique. Such mixing of interior ocean water near the continental slope could prove important to global mixing processes and cannot be neglected. We believe insights such as this can be obtained only from synoptic two-dimensional, or even three-dimensional, representations of mixing. The ability to routinely make large-scale synoptic surveys of mixing will be vital to the next generation of regional- and global-scale modeling efforts.

Acknowledgments. We thank Mark Willis and Linda Fayler, OSU Marine Technicians, who were responsible for the highly successful SeaSoar operations, and Robert O'Malley, who processed the SeaSoar SeaBird CTD data for use in calibrating the MicroSoar sensors. The officers, mates, and crew of the R/V *Endeavor* performed superbly, allowing us to tow SeaSoar through a region with considerable shipping traffic and fishing activity. We also thank Kieran O'Driscoll and Andrew Dale, who were in charge of assembling and mounting MicroSoar on SeaSoar. The helpful comments and suggestions given by two anonymous reviewers are appreciated. This work was funded by Office of Naval Research Grants N00014-94-1-0325 and N00014-95-1-0382, and by NSF Grant OCE-0002758.

REFERENCES

Barth, J. A., D. Bogucki, S. D. Pierce, and M. Kosro, 1998: Secondary circulation associated with a shelf break front. *Geophys. Res. Lett.,* **25,** 2761–2764.

Batchelor, G. K., 1959: Small-scale variation of convected quantities like temperature in turbulent fluid. *J. Fluid Mech.,* **5,** 113–133.

Bryan, F., 1987: Parameter sensitivity of primitive equation ocean general circulation models. *J. Phys. Oceanogr.,* **17,** 970–985.

Caldwell, D. R., T. M. Dillon, and J. N. Moum, 1985: The rapid-sampling vertical profiler: An evaluation. *J. Atmos. Oceanic Technol.* **2,** 615–625.

Dillon, T. M., 1984: The energetics of overturning structure: Implications for the theory of fossil turbulence. *J. Phys. Oceanogr.,* **14,** 541–549.

——, and D. R. Caldwell, 1980: The Batchelor spectrum and dissipation in the upper ocean. *J. Geophys. Res.,* **85,** 1910–1916.

Erofeev, A. Y., T. M. Dillon, J. A. Barth, and G. H. May, 1998: MicroSoar microstructure observations during the Coastal Mixing and Optics Experiment: R/V Endeavor cruises from 14-August to 1-September 1996 and 25-April to 15-May 1997. College of Oceanic and Atmospheric Sciences, Oregon State University, Ref. 98–3, Data Report 170, 375 pp.

Grant, H. L. R., R. W. Stewart, and A. Moilliet, 1962: Turbulence spectra from a tidal channel. *J. Fluid Mech.,* **12,** 241–263.

Gregg, M. C., 1976: Temperature and salinity microstructure in the Pacific Equatorial Undercurrent. *J. Geophys. Res.,* **81,** 1180–1196.

——, 1987: Diapycnal mixing in the thermocline: A review. *J. Geophys. Res.,* **92,** 5249–5286.

——, 1998: Estimation and geography of diapycnal mixing in the stratified ocean. *Physical Processes in Lakes and Oceans,* Vol. 54, J. Imberger, Ed., Amer. Geophys. Union, 305–338.

Ledwell, J. R., A. J. Watson, and C. S. Law, 1993: Evidence for slow mixing across the pycnocline from an open-ocean tracer release experiment. *Nature,* **364,** 701–703.

Lueck, R. G., F. Wolk, and H. Yamazaki, 2002: Oceanic velocity microstructure measurements in the 20th century: A review. *J. Oceanogr.,* **58**, Oceanographic Society of Japan, 153–174.

May, G. H., 1997: MicroSoar: A high-speed microstructure profiling system. M.S. thesis, College of Oceanic and Atmospheric Sciences, Oregon State University, 227 pp.

Moum, J. N., and D. R. Caldwell, 1985: Local influences of shear-flow turbulence in the equatorial ocean. *Science,* **230,** 315–316.

Nash, D. N., and J. N. Moum, 1999: Estimating salinity variance dissipation rate from conductivity microstructure measurements. *J. Atmos. Oceanic Technol.,* **16,** 1474–1482.

O'Malley, R. J., J. A. Barth, A. Erofeev, J. Fleischbein, P. M. Kosro, and S. D. Pierce, 1998: SeaSoar CTD observations during the Coastal Mixing and Optics Experiment: R/V Endeavor cruises from 14-August to 1-September 1996 and 25-April to 15-May 1997. College of Oceanic and Atmospheric Sciences, Oregon State University, Ref. 98–1, Data Report 168, 499 pp.

Osborn, T. R., 1980: Estimates of the local rate of vertical diffusion from dissipation measurements. *J. Phys. Oceanogr.,* **10,** 83–89.

Padman, L., and T. M. Dillon, 1991: Turbulent mixing near the Yermak Plateau during the Coordinated Eastern Arctic Experiment. *J. Geophys. Res.,* **96,** 4769–4782.

Paka, V. T., V. N. Nabatov, I. D. Lozovatsky, and T. M. Dillon, 1999: Oceanic microstructure measurements by ''Baklan'' and ''Grif.'' *J. Atmos. Oceanic Technol.,* **16,** 1519–1532.

Pollard, R., 1986: Frontal surveys with a towed profiling conductivity/temperature/depth measurement package (SeaSoar). *Nature,* **323,** 433–435.

Toole, J. M., K. L. Polzin, and R. W. Schmitt, 1994: Estimates of mixing in the abyssal ocean. *Science,* **264,** 1120–1123.

UNESCO, 1981: Background papers and supporting data on the international equation of state of seawater, 1980. UNESCO Tech. Paper in Mar. Sci., No. 38, 192 pp.

Vachon, P., and R. G. Lueck, 1984: A small combined temperature and conductivity probe. *Proc. 1984 STD Conf. and Workshop,* San Diego, CA, Marine Technology Society and the MPS Oceanic Instrumentation Committee, 126–131.

Washburn, L., T. F. Duda, and D. C. Jacobs, 1996: Interpreting conductivity microstructure: Estimating the temperature variance dissipation rate. *J. Atmos. Oceanic Technol.,* **13,** 1166–1188.

Wijesekera, H., L. Padman, T. Dillon, M. Levine, C. Paulson, and R. Pinkel, 1993: The application of internal-wave dissipation models to a region of strong mixing. *J. Phys. Oceanogr.,* **23,** 269–286.